

# Spin Dynamics in Hierarchical Black Hole Triples: Predicting Final Spin-Orbit Misalignment Angle From Initial Conditions

YUBO SU,<sup>1</sup> DONG LAI,<sup>1</sup> AND BIN LIU<sup>1</sup>

<sup>1</sup>*Cornell Center for Astrophysics and Planetary Science, Department of Astronomy, Cornell University, Ithaca, NY 14853, USA*

(Received XXXX; Revised XXXX; Accepted XXXX)

Submitted to ApJ

## ABSTRACT

Abstract

*Keywords:* keywords

## 1. INTRODUCTION

As the Laser Interferometer Gravitational-wave Observatory (LIGO) continues to detect mergers of black hole (BH) binaries (e.g. Abbott et al. 2020, 2017b,a,c, 2016c,a,b), it is increasingly important to systematically study various formation channels of BH binaries and their observable signatures. The canonical channel consists of isolated binary evolution, in which mass transfer and friction in the common envelope phase cause the binary orbit to shrink sufficiently that it subsequently merges via emission of gravitational waves (GW) within a Hubble time (e.g. Dominik et al. 2012). BH binaries formed via isolated binary evolution are expected to be slowly rotating (Fuller & Ma 2019).

However, (Graham et al. 2020) reports that the GW event candidate S190521g has at least one significantly spinning component. This is consistent with the tertiary-induced dynamical formation channel, in which a BH binary that is too far separated to merge in isolation is induced to merge by a tertiary companion, often a supermassive black hole (SMBH). The SMBH induces Lidov-Kozai (LK) oscillations in the BH binary that excite the eccentricity to very large values, which causes significant GW emission at pericenter that allows the BH binary to coalesce and merge within a Hubble time.

Because eccentricity is efficiently damped by gravitational wave (GW) radiation, the vast majority of BH binaries are expected to be circular when entering the LIGO sensitivity band regardless of their formation channel. It has been suggested that the BH spin and the spin-orbit misalignment angle may carry information on the binary formation history. In partic-

ular, through the phase shift in the binary inspiral waveform, one can directly measure the mass-weighted average of the dimensionless spin parameter

$$\chi_{\text{eff}} \equiv \frac{m_1 \chi_1 + m_2 \chi_2}{m_1 + m_2} \cdot \hat{\mathbf{L}}, \quad (1)$$

where  $m_{1,2}$  are the masses of the BHs,  $\chi_{1,2} = c\mathbf{S}_{1,2}/(Gm_{1,2}^2)^2$  are the dimensionless BH spins, and  $\hat{\mathbf{L}}$  is the unit orbital angular momentum vector.

In a recent paper, Liu & Lai (2018) found that LK-induced mergers can often yield a 90° spin attractor: when the inner binary starts with  $\theta_{\text{sl}}^i = 0$ , the individual BH spins often evolve towards spin-orbit misalignment angle  $\theta_{\text{sl}}^f = 90^\circ$ , where  $\theta_{\text{sl}}$  is the angle between the BH spin and  $\hat{\mathbf{L}}$ . They found that the attractor exists when (i) the LK-induced orbital decay is slow, and (ii) the octupole effect is unimportant. Fig. 1 gives an example of this attractor, where  $\theta_{\text{sl}}$  rapidly converges to  $\approx 90^\circ$  at late times in the bottom right panel. Fig. 2 shows how  $\theta_{\text{sl}}^f$  varies when the initial inclination of the inner orbit  $I_0$  (relative to the tertiary orbit) is varied. Note that for longer merger times, corresponding to  $I_0$  farther from 90°, the final  $\theta_{\text{sl}}^f \approx 90^\circ$ . In both of these plots, the tertiary's eccentricity is taken to be zero, for which octupole effects are negligible.

The physical origin of this 90° attractor is not well understood. Liu & Lai (2018) proposed an explanation based on analogy with an adiabatic invariant in systems where the inner binary remains circular through the inspiral (Liu & Lai 2017). However, this analogy is not justified, as significant eccentricity excitation is a necessary ingredient in LK-induced mergers. In addition, the results in Liu & Lai (2017) show no 90° attractor even though the orbital evolution is slow and regular.

In this paper, we study an analytic theory that reproduces the 90° attractor as well as its regime of validity. In Sections 2

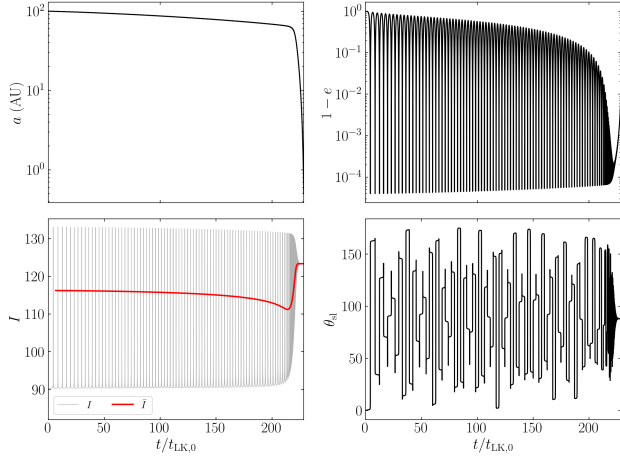


**Figure 1.** Orbital and spin evolution in a system for which the total change in the adiabatic invariant  $\bar{\theta}_e$  is  $\lesssim 0.01^\circ$ . The unit of time  $t_{\text{LK},0}$  is the LK timescale [Eq. (8)] evaluated for the initial conditions. The inner binary is taken to have  $a = 100$  AU,  $m_1 = 30M_\odot$ ,  $m_2 = 20M_\odot$ ,  $I_0 = 90.35^\circ$ , and  $e_0 = 0.001$ , while the tertiary SMBH has  $\tilde{a}_3 = 2.2$  pc,  $m_3 = 3 \times 10^7 M_\odot$ . We take  $\theta_{\text{sl}}^i = 0$ . The top two panels show  $a$  and  $e$  respectively. The bottom two panels show the inclination of the inner binary, both instantaneous ( $I$ ) and appropriately averaged following Eq. (31) ( $\bar{I}$ ), and the instantaneous spin-orbit misalignment angle  $\theta_{\text{sl}}$ .

and 3, we set up the relevant equations of motion for the orbital and spin evolution of the system. In Sections 4 and 5, we develop an analytic theory and compute its regime of validity for LK-induced mergers. In Section 6, we comment on the consistency of our results with Liu & Lai (2017). We discuss and conclude in Section 7.

## 2. LK-INDUCED MERGERS: ORBITAL EVOLUTION

We study Lidov-Kozai (LK) oscillations due to an external perturber to quadrupole order and include apsidal precession and gravitational wave radiation due to general relativity. Consider an black hole (BH) binary with masses  $m_1$  and  $m_2$  having total mass  $m_{12}$  and reduced mass  $\mu$  orbiting a supermassive black hole (SMBH) with mass  $m_3 \gg m_1$  and  $m_2$ . Call  $a_3$  and  $e_3$  the semimajor axis and eccentricity of the orbit of the inner binary around the SMBH, and define effective semimajor axis

$$\tilde{a}_3 \equiv a_3 \sqrt{1 - e_3^2}. \quad (2)$$

Finally, call  $\mathbf{L}_{\text{out}} \equiv L_{\text{out}} \hat{\mathbf{L}}_{\text{out}}$  the angular momentum of the SMBH relative to the center of mass of the inner BH binary, and call  $\mathbf{L} \equiv L \hat{\mathbf{L}}$  the orbital angular momentum of the inner BH binary. We take  $\mathbf{L}_{\text{out}}$  to be fixed.

We then consider the motion of the inner binary, described by the Keplerian orbital elements ( $a, e, \varphi, I, \omega$ ) (respectively: semimajor axis, eccentricity, longitude of the ascending node, inclination, and argument of periapsis). The equations describing the motion of these orbital elements are (Peters 1964;

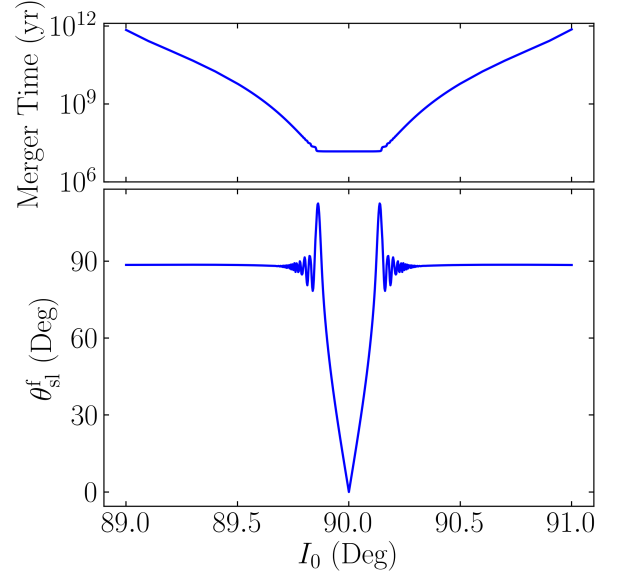


**Figure 2.** Plot of merger time of the inner binary and  $\theta_{\text{sl}}^f$  for  $m_1 = 30M_\odot$ ,  $m_2 = 20M_\odot$ ,  $m_3 = 3 \times 10^7 M_\odot$ ,  $a_{\text{in}} = 100$  AU,  $\tilde{a}_3 = 2.2$  pc,  $e_3 = 0$ , where  $e_0 = 0.001$  and  $\theta_{\text{sl}}^i = 0$  over a restricted range of  $I_0$  (analogous to the bottom-most panel in Fig. 3 of Liu & Lai 2018), where the blue line is taken from numerical simulations. It is clear that for  $I_0$  sufficiently far from  $90^\circ$ , the resulting  $\theta_{\text{sl}}^f$  are quite similar and are near  $90^\circ$  (Liu & Lai 2018).

Storch & Lai 2015; Liu & Lai 2018)

$$\frac{da}{dt} = \left( \frac{da}{dt} \right)_{\text{GW}}, \quad (3)$$

$$\frac{de}{dt} = \frac{15}{8t_{\text{LK}}} e \sqrt{1 - e^2} \sin 2\omega \sin^2 I + \left( \frac{de}{dt} \right)_{\text{GW}}, \quad (4)$$

$$\frac{d\varphi}{dt} = \frac{3}{4t_{\text{LK}}} \frac{\cos I (5e^2 \cos^2 \omega - 4e^2 - 1)}{\sqrt{1 - e^2}}, \quad (5)$$

$$\frac{dI}{dt} = \frac{15}{16} \frac{e^2 \sin 2\omega \sin 2I}{\sqrt{1 - e^2}}, \quad (6)$$

$$\frac{d\omega}{dt} = \frac{3}{4t_{\text{LK}}} \frac{2(1 - e^2) + 5 \sin^2 \omega (e^2 - \sin^2 I)}{\sqrt{1 - e^2}} + \Omega_{\text{GR}}, \quad (7)$$

where we define

$$t_{\text{LK}}^{-1} = n \left( \frac{m_3}{m_{12}} \right) \left( \frac{a}{\tilde{a}_3} \right)^3, \quad (8)$$

$$\left( \frac{da}{dt} \right)_{\text{GW}} = - \frac{a}{t_{\text{GW}}(e)}, \quad (9)$$

$$t_{\text{GW}}^{-1}(e) = \frac{64}{5} \frac{G^3 \mu m_{12}^2}{c^5 a^4} \frac{1}{(1-e^2)^{7/2}} \left( 1 + \frac{73}{24} e^2 + \frac{37}{96} e^4 \right), \quad (10)$$

$$\left( \frac{de}{dt} \right)_{\text{GW}} = - \frac{304}{15} \frac{G^3 \mu m_{12}^2}{c^5 a^4} \frac{1}{(1-e^2)^{5/2}} \left( 1 + \frac{121}{304} e^2 \right), \quad (11)$$

$$\Omega_{\text{GR}}(e) = \frac{3Gnm_{12}}{c^2 a (1-e^2)}, \quad (12)$$

and  $n = \sqrt{Gm_{12}/a^3}$  is the mean motion of the inner binary. We will often refer to  $e_{\min}$  and  $e_{\max}$  the minimum/maximum eccentricity in a single LK cycle and notate  $j(e) = \sqrt{1-e^2}$ .

For concreteness, we adopt fiducial parameters similar to those from Liu & Lai (2018): the inner binary has  $a = 100$  AU,  $m_1 = 30M_{\odot}$ ,  $m_2 = 20M_{\odot}$ , and initial  $e_0 = 0.001$  with varying  $I_0$ . We take the SMBH tertiary companion to have  $m_3 = 3 \times 10^7 M_{\odot}$  and  $\tilde{a}_3 = 4.5 \times 10^5$  AU = 2.2 pc. This gives the same  $t_{\text{LK}}$  as do the parameters used in Liu & Lai (2018). We refer to this as the fiducial parameter regime, and all simulations use these parameters unless otherwise noted.

We summarize a few key analytical properties of this orbital evolution below:

- Neglecting GR effects (GW radiation and apsidal precession), the above equations describe periodic oscillations in  $e$  and  $I$ . There are two conserved quantities, the total angular momentum  $\mathbf{L}_{\text{out}} + \mathbf{L}$  and the “Kozai constant” (Lidov 1962; Kozai 1962):

$$K \equiv j(e) \cos I. \quad (13)$$

This implies that  $e$  is a function of  $\omega$  only (Kinoshita 1993; Storch & Lai 2015).

Note that an eccentricity maximum occurs every half-period of  $\omega$ , at  $\omega = \pi/2$  and  $\omega = 3\pi/2$  (Kinoshita 1993; Storch & Lai 2015). It is most convenient to define the LK period  $P_{\text{LK}}$  as the *half*-period of  $\omega$ , and the corresponding frequency  $\Omega_{\text{LK}}$ :

$$\pi = \int_0^{P_{\text{LK}}} \frac{d\omega}{dt} dt, \quad (14)$$

$$\Omega_{\text{LK}} \equiv \frac{2\pi}{P_{\text{LK}}}. \quad (15)$$

The conservation laws above can be combined to calculate the maximum eccentricity as a function of  $I$ . If the

minimum eccentricity is negligible and the inclination at the start of the LK cycle is  $I_0$ , then

$$e_{\max} \equiv \sqrt{1 - \frac{5}{3} \cos^2 I_0}. \quad (16)$$

Note that these results assume  $L_{\text{out}} \gg L$  and that both octupole and GR effects are negligible; see Liu & Lai (2018) for generalized forms of the above results.

Finally, when  $e_{\min} \ll e_{\max}$ , the binary spends a fraction  $\sim j(e_{\max})$  of the LK cycle near  $e \simeq e_{\max}$  (Anderson et al. 2016).

- When GR effects are considered, the system gradually coalesces due to GW radiation, primarily in the  $j(e_{\max})P_{\text{LK}}$  window at eccentricity maxima. During this process, there are three competing timescales: (i)  $\Omega_{\text{L}}$  precession driven by the tertiary ( $\sim t_{\text{LK}}$ ), (ii) apsidal precession due to post-Newtonian effects ( $\sim \Omega_{\text{GR}}^{-1}(e_{\max})/j(e_{\max})$ ), and (iii) orbital decay due to GW radiation ( $\sim t_{\text{GW}}(e_{\max})/j(e_{\max})$ ). At early times, (i) is the shortest, but as  $a$  decreases, (ii) and (iii) become dominant and eccentricity oscillations become suppressed, which we term “eccentricity freezing”. We consider the two conditions under which this happens.

Apsidal precession becomes important when  $\Omega_{\text{GR}}$  is the dominant contribution in Eq. (7). Quantitatively, this occurs when

$$\frac{\epsilon_{\text{GR}}}{j(e_{\max})} \gg 1, \quad (17)$$

where we define

$$\epsilon_{\text{GR}} \equiv \frac{3Gm_{12}^2 \tilde{a}_3^3}{c^2 m_3 a^4}. \quad (18)$$

GW radiation can also inhibit eccentricity oscillations when  $t_{\text{LK}} j(e) \gtrsim t_{\text{GW}}(e)$  [see Eq. (4)]. In order for GW radiation to be the dominant cause of eccentricity freezing, we require

$$1 \lesssim \frac{t_{\text{GW}}^{-1}(e)}{\Omega_{\text{GR}}} \sim \left( \frac{Gm_{12}}{a(1-e^2)c^2} \right)^{3/2} \frac{1}{1-e^2}, \quad (19)$$

$$\sim \left( \frac{v_p}{c} \right)^3 \frac{1}{1-e^2}, \quad (20)$$

where  $v_p$  is the pericenter velocity of the inner binary. Since  $v_p/c \ll 1$ , we find that apsidal precession is usually more effective at freezing the eccentricity.

The behavior of  $a$ ,  $e$ , and  $I$  for a characteristic LK-induced merger can be seen in Fig. 1. At early times,  $e$  and  $I$  have large oscillations while  $a$  slowly decreases. At later times,  $e$  and  $I$  stop oscillating as apsidal precession freezes the eccentricity,

and both  $a$  and  $e$  decrease under GW radiation. Since  $P_{\text{LK}}$  is defined as the half-period in  $\omega$ ,  $\Omega_{\text{LK}}$  asymptotes to  $\Omega_{\text{GR}}$  at late times even though the eccentricity is frozen (bottom right panel of Fig. 1).

### 3. SPIN DYNAMICS: EQUATIONS

We are ultimately interested in the spin orientations of the inner BHs at merger as a function of initial conditions. Since they evolve independently to leading post-Newtonian order, we focus on the dynamics of a single BH spin  $\hat{\mathbf{S}}$ . Since the spin magnitude does not enter into the dynamics, we write  $\mathbf{S} \equiv \hat{\mathbf{S}}$  for brevity (i.e.  $\mathbf{S}$  is a unit vector). Neglecting spin-spin interactions,  $\mathbf{S}$  undergoes de Sitter precession about  $\mathbf{L}$  as

$$\frac{d\mathbf{S}}{dt} = \Omega_{\text{SL}} \hat{\mathbf{L}} \times \mathbf{S}, \quad (21)$$

$$\Omega_{\text{SL}} = \frac{3Gn(m_2 + \mu/3)}{2c^2 a (1 - e^2)}. \quad (22)$$

To analyze the dynamics of the spin vector, we go to co-rotating frame with  $\hat{\mathbf{L}}$  about  $\hat{\mathbf{L}}_{\text{out}}$ , where Eq. (21) becomes

$$\left( \frac{d\mathbf{S}}{dt} \right)_{\text{rot}} = (\Omega_{\text{L}} \hat{\mathbf{L}}_{\text{out}} + \Omega_{\text{SL}} \hat{\mathbf{L}}) \times \mathbf{S}, \quad (23)$$

$$= \Omega_{\text{e}} \times \mathbf{S}, \quad (24)$$

where we define

$$\Omega_{\text{e}} \equiv \Omega_{\text{L}} \hat{\mathbf{L}}_{\text{out}} + \Omega_{\text{SL}} \hat{\mathbf{L}}, \quad (25)$$

$$\Omega_{\text{L}} \equiv -\frac{d\phi}{dt}. \quad (26)$$

#### 3.1. Nondissipative Dynamics

Despite its simple form, Eq. (24) is difficult to analyze, since  $\Omega_{\text{e}}$  varies significantly within each LK cycle and evolves over timescale  $\sim t_{\text{GW}}(e)$ . For simplicity, we first consider the limit where dissipation via GW radiation can be completely neglected ( $t_{\text{GW}}(e) \rightarrow \infty$ ). Then  $\Omega_{\text{e}}$  is exactly periodic with period  $P_{\text{LK}}$ . We can rewrite Eq. (24) in Fourier components

$$\left( \frac{d\mathbf{S}}{dt} \right)_{\text{rot}} = \left[ \bar{\Omega}_{\text{e}} + \sum_{N=1}^{\infty} \Omega_{\text{e}N} \cos(N\Omega_{\text{LK}}t) \right] \times \mathbf{S}. \quad (27)$$

We write  $\bar{\Omega}_{\text{e}} \equiv \Omega_{\text{e}0}$  for convenience, where the bar denotes an average over an LK cycle. We adopt the convention where  $t = 0$  is the time of maximum eccentricity of the LK cycle.

This system resembles that studied in Storch & Lai (2015), where a star's obliquity varies chaotically when driven by a hot Jupiter undergoing LK oscillations. One strong indicator of chaos in their study is the presence of fine structure in a bifurcation diagram [Fig. 1 of Storch & Lai (2015)] that shows the oscillation amplitude of a misalignment angle  $\theta_{\text{sl}}$  when varying system parameters in the “transadiabatic” regime,

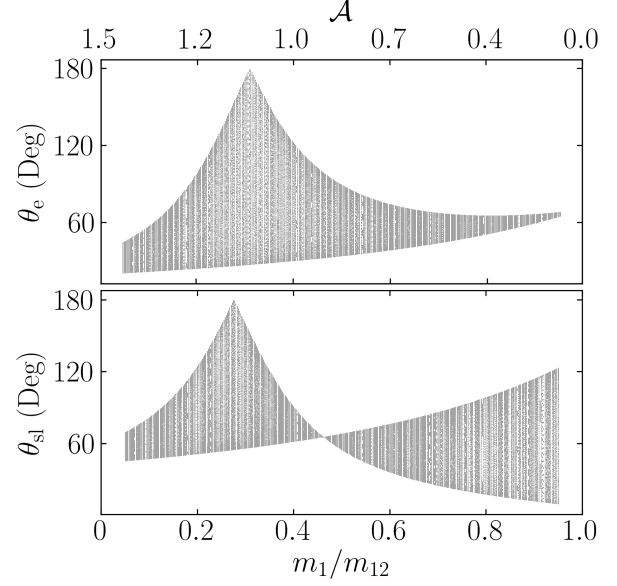


**Figure 3.** Bifurcation diagram for  $I_0 = 70^\circ$ , for physical parameters  $m_1 + m_2 = 60M_\odot$ ,  $m_3 = 3 \times 10^7 M_\odot$ ,  $a_{\text{in}} = 0.1$  AU,  $\tilde{a}_3 = 300$  AU, and  $e_3 = 0$ . For each mass ratio  $m_1/m_{12}$ , Eq. (24) is solved over 500 LK cycles, and both  $\theta_{\text{e}}$  and  $\theta_{\text{sl}}$  are sampled at every eccentricity maximum and are plotted. The top axis shows the adiabaticity parameter  $\mathcal{A}$  as defined by Eq. (33), the natural adiabaticity parameter for this problem. Interesting behavior is expected for  $\mathcal{A} \approx 1$ .

where some adiabaticity parameter crosses 1. In our system, the most natural angle to examine is

$$\cos \theta_{\text{e}} = \frac{\bar{\Omega}_{\text{e}}}{\Omega_{\text{e}}} \cdot \mathbf{S}. \quad (28)$$

To generate an analogous bifurcation diagram for our problem, we begin with  $\mathbf{S} \parallel \mathbf{L}$ , then evolve Eq. (24) while sampling both  $\theta_{\text{sl}}$  and  $\theta_{\text{e}}$  at eccentricity maxima. We repeat this procedure while varying the mass ratio  $m_1/m_{12}$  of the inner binary, which only changes  $\Omega_{\text{SL}}$  without changing the orbital evolution. Note that the fiducial parameters do not serve this purpose well because GR effects are too weak initially, and the system is not in the desired regime. Our choice of parameters and our results are shown in Fig. 3.

While our bifurcation diagram has some structure, it does not exhibit small scale variability, suggesting that Eq. (24) cannot generate chaotic behavior. We can understand this using Floquet theory, as Eq. (24) is a linear system with periodic coefficients (the system studied in SL15 is nonlinear). Floquet’s theorem says that when a linear system with periodic coefficients is integrated over a period, the evolution can be described by a linear transformation, the *monodromy matrix*  $\tilde{\mathbf{M}}$ , or

$$\mathbf{S}(t + P_{\text{LK}}) = \tilde{\mathbf{M}}\mathbf{S}(t), \quad (29)$$

where  $\tilde{\mathbf{M}}$  is independent of  $\mathbf{S}$ .

While  $\tilde{\mathbf{M}}$  can be easily defined, it cannot be evaluated in closed form. Thankfully, it suffices to reason directly about the properties of  $\tilde{\mathbf{M}}$ . In our problem,  $\mathbf{M}$  must be a proper orthogonal matrix, or a rotation matrix, as it represents the effect of many infinitesimal rotations about  $\Omega_e$ <sup>1</sup>. Therefore, every  $P_{LK}$ , the dynamics of Eq. (24) are equivalent to a rotation about a fixed axis, prohibiting chaotic behavior.

One other traditional indicator of chaos is a positive Lyapunov exponent, obtained when the separation between nearby trajectories diverges *exponentially* in time. In Floquet theory, the Lyapunov exponent is the logarithm of the largest eigenvalue of the monodromy matrix. Since  $\tilde{\mathbf{M}}$  is a rotation matrix here, the Lyapunov exponent must be 0, indicating no chaos. Numerically, we were able to verify the separation between nearby trajectories does not grow in time.

### 3.2. With GW Dissipation

When  $t_{GW}$  is finite, the coefficients  $\Omega_{eN}$  change over timescales  $\sim t_{GW}(e_{\max})/j(e_{\max})$  (see discussion in Section 2). However, when the system satisfies both  $t_{GW}(e_{\max}) \gg \Omega_{GR}^{-1}(e_{\max})$  and  $t_{LK}j(e_{\max})$ , we can approximate its evolution as a sequence of nondissipative LK cycles. This is a good approximation when coalescence takes place over more than a few  $P_{LK}$ , which is the case for most of the systems we study here.

Once  $a$  is sufficiently small that  $\Omega_{SL} \gg \Omega_L$  (this also gives  $\epsilon_{GR} \gg 1$ , implying the LK cycles are suppressed), it can be seen from Eq. (24) that  $\theta_e = \theta_{sl}$  is constant (see bottom right panel of Fig. 1). For the fiducial parameters, we stop the simulation at  $a \leq 0.5$  AU, as  $\theta_{sl}$  has converged to its final value.

### 3.3. Component Form

For later analysis, it is also useful to write Eq. (27) in components. To do so, it is next useful to define inclination angle  $\bar{I}_e$  as the angle between  $\bar{\Omega}_e$  and  $\mathbf{L}_{out}$  as shown in Fig. 4. To express  $\bar{I}_e$  algebraically, we first define LK-averaged quantities

$$\overline{\Omega_{SL} \sin I} \equiv \bar{\Omega}_{SL} \sin \bar{I}, \quad (30)$$

$$\overline{\Omega_{SL} \cos I} \equiv \bar{\Omega}_{SL} \cos \bar{I}. \quad (31)$$

It then follows that

$$\tan \bar{I}_e = \frac{\mathcal{A} \sin \bar{I}}{1 + \mathcal{A} \cos \bar{I}}, \quad (32)$$

where

$$\mathcal{A} \equiv \frac{\bar{\Omega}_{SL}}{\bar{\Omega}_L}. \quad (33)$$

<sup>1</sup> More formally,  $\tilde{\mathbf{M}} = \tilde{\Phi}(P_{LK})$  where  $\tilde{\Phi}(t)$  is the *principal fundamental matrix solution*: the columns of  $\tilde{\Phi}$  are solutions to Eq. (24) and  $\tilde{\Phi}(0)$  is the identity. By linearity, the columns of  $\tilde{\Phi}(t)$  remain orthonormal, while its determinant does not change, so  $\tilde{\mathbf{M}}$  is a proper orthogonal matrix, or a rotation matrix.

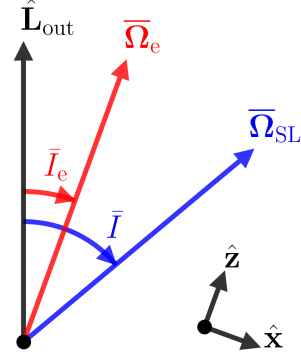


**Figure 4.** Definition of angles, shown in plane of the two angular momenta  $\mathbf{L}_{out}$  and  $\mathbf{L}$ . Note that for  $I_0 > 90^\circ$  (and  $\bar{I} > 90^\circ$ ), we have  $\bar{I}_e < 0$  since  $\Omega_L < 0$ . The bottom right shows our choice of coordinate axes.

We now can choose non-inertial coordinate system where  $\hat{z} \propto \bar{\Omega}_e$  and  $\hat{x}$  lies in the plane of  $\mathbf{L}_{out}$  and  $\mathbf{L}$  with positive component along  $\mathbf{L}$  (see Fig. 4). In this reference frame, the polar coordinate is just  $\bar{\theta}_e$  as defined above in Eq. (38), and the equation of motion becomes

$$\frac{d\mathbf{S}}{dt} = \left[ \bar{\Omega}_e \hat{z} + \sum_{N=1}^{\infty} \Omega_{eN} \cos(N\Omega_{LK}t) \right] \times \mathbf{S} - \dot{I}_e \hat{y} \times \mathbf{S}. \quad (34)$$

One further simplification lets us cast this vector equation of motion into scalar form. Break  $\mathbf{S}$  into components  $\mathbf{S} = S_x \hat{x} + S_y \hat{y} + \cos \bar{\theta}_e \hat{z}$  and define complex variable

$$S_{\perp} \equiv S_x + iS_y. \quad (35)$$

Then, we can rewrite Eq. (34) as

$$\begin{aligned} \frac{dS_{\perp}}{dt} = & i\bar{\Omega}_e S_{\perp} - \dot{I}_e \cos \bar{\theta}_e + \sum_{N=1}^{\infty} [\cos(\Delta I_{eN}) S_{\perp} \\ & - i \cos \theta \sin(\Delta I_{eN})] \Omega_{eN} \cos N\Omega_{LK}t. \end{aligned} \quad (36)$$

Here, for each  $\Omega_{eN}$  Fourier harmonic, we denote its magnitude  $\Omega_{eN}$  and its inclination angle relative to  $\mathbf{L}_{out}$  as  $I_{eN}$  using the same convention as Fig. 4 (where  $\bar{I}_e \equiv I_{e0}$ ), and  $\Delta I_{eN} = \bar{I}_e - I_{eN}$ .

## 4. ANALYSIS: DEVIATION FROM ADIABATICITY

In general, Eq. (27) is difficult to study analytically. Two approximations can be made: (i) the effect of the  $N \geq 1$  harmonic terms is negligible, and the dominant effect in the system is motion of  $\bar{\Omega}_e$ ; or (ii) the  $\Omega_{eN}$  Fourier coefficients are nonnegligible, and the dominant effect in the system arises from resonant interactions due to the Fourier coefficients. In this section, we analyze the former approximation and provide accurate analytic descriptions of dynamics. The effect of the harmonic terms is studied in Section 5.



#### 4.1. The Adiabatic Invariant

When neglecting the  $N \geq 1$  harmonic terms, the equation of motion is modified to

$$\left( \frac{d\bar{\mathbf{S}}}{dt} \right)_{\text{rot}} = \bar{\boldsymbol{\Omega}}_e \times \bar{\mathbf{S}}. \quad (37)$$

It is not obvious in what capacity analysis of Eq. (37) is applicable to Eq. (27). Empirically, we find that the LK-average of  $\mathbf{S}$  (which has magnitude  $\leq 1$ ) often evolves following Eq. (37), motivating our notation  $\bar{\mathbf{S}}$ . Over timescales  $\lesssim P_{\text{LK}}$ , Eq. (37) loses accuracy as the evolution of  $\mathbf{S}$  itself is dominated by the  $N \geq 1$  harmonics we have neglected. An intuitive interpretation of this result is that the  $N \geq 1$  harmonics vanish when integrating Eq. (27) over an LK cycle.

Eq. (37) has one desirable property:  $\bar{\theta}_e$ , given by

$$\cos \bar{\theta}_e \equiv \bar{\mathbf{S}} \cdot \frac{\bar{\boldsymbol{\Omega}}_e}{\bar{\Omega}_e}, \quad (38)$$

is an adiabatic invariant. The adiabaticity condition requires the precession axis evolve slowly compared to the precession frequency at all times:

$$\frac{d\bar{I}_e}{dt} \ll \bar{\Omega}_e. \quad (39)$$

For the simulation shown in Fig. 1, the values of  $\dot{\bar{I}}_e$  and  $\bar{\Omega}_e$  are shown in the top panel of Fig. 5. Note that  $\dot{\bar{I}}_e \ll \bar{\Omega}_e$  at all times, and the total change in  $\bar{\theta}_e$  in this simulation is  $0.01^\circ$ , small as expected.

#### 4.2. Calculating Deviation from Adiabaticity

In real systems, the particular extent to which  $\bar{\theta}_e$  is conserved depends on how well Eq. (39) is satisfied. In this subsection, we derive a loose bound on the total non-conservation of  $\bar{\theta}_e$ , then in the next subsection we show this bound can be estimated from initial conditions.

When neglecting harmonic terms, the scalar equation of motion Eq. (36) becomes

$$\frac{dS_\perp}{dt} = i\bar{\Omega}_e S_\perp - \dot{\bar{I}}_e \cos \bar{\theta}_e. \quad (40)$$

This can be solved in closed form using an integrating factor. Defining

$$\Phi(t) \equiv \int^t \bar{\Omega}_e dt, \quad (41)$$

we obtain solution up between initial time  $t_i$  and final time  $t_f$

$$e^{-i\Phi} S_\perp \Big|_{t_i}^{t_f} = - \int_{t_i}^{t_f} e^{-i\Phi(\tau)} \dot{\bar{I}}_e \cos \bar{\theta} d\tau. \quad (42)$$

Recalling  $|S_\perp| = \sin \bar{\theta}_e$  and analyzing Eq. (42), we see that  $\bar{\theta}_e$  oscillates about its initial value  $\bar{\theta}_e^i$  with amplitude

$$|\Delta \bar{\theta}_e| \sim \frac{\dot{\bar{I}}_e}{\bar{\Omega}_e}. \quad (43)$$

It can be seen that, in the adiabatic limit [Eq. (39)],  $\bar{\theta}_e$  is indeed conserved, as the right hand side goes to zero.

This is compared to the  $\Delta \bar{\theta}_e$  for the fiducial simulation in the bottom panel of Fig. 5. Note that  $\bar{\theta}_e$  is indeed mostly constant where Eq. (43) predicts small oscillations.

Furthermore, if we denote  $|\Delta \bar{\theta}_e|^f$  to be the total change in  $\bar{\theta}_e$  over  $t \in [t_i, t_f]$ , we can give loose bound<sup>2</sup>

$$|\Delta \bar{\theta}_e|^f \lesssim \left| \frac{\dot{\bar{I}}_e}{\bar{\Omega}_e} \right|_{\text{max}}. \quad (44)$$

Inspection of Fig. 5 indicates that the dynamics are mostly uninteresting except near the peak of  $\dot{\bar{I}}_e$ , which is where  $\Omega_{\text{SL}} \simeq \Omega_{\text{L}}$ . We present a zoomed in view of the behavior of all dynamical quantities near the peak of  $\dot{\bar{I}}_e$  in the fiducial simulation in Fig. 6. In particular, in the bottom-rightmost plot, we see that the fluctuations in  $\bar{\theta}_e$  are dominated by a second contribution, the subject of the discussion in Section 5. For comparison, we show a more rapid coalescence, where  $I_0 = 90.2^\circ$ , for which  $|\Delta \bar{\theta}_e|^f \approx 2^\circ$ , in Fig. 7. If we again examine the bottom-rightmost plot, we see that the fluctuations in  $\Delta \bar{\theta}_e$  are somewhat better described by Eq. (43).

#### 4.3. Estimate of Deviation from Adiabaticity from Initial Conditions

To estimate  $\left| \dot{\bar{I}}_e / \bar{\Omega}_e \right|_{\text{max}}$  from initial conditions, we first differentiate Eq. (32),

$$\dot{\bar{I}}_e = \left( \frac{\mathcal{A}}{\bar{\mathcal{A}}} \right) \frac{\mathcal{A} \sin \bar{I}}{1 + 2\mathcal{A} \cos \bar{I} + \mathcal{A}^2}. \quad (45)$$

It also follows from Eq. (25) that

$$\bar{\Omega}_e = \bar{\Omega}_{\text{L}} \left( 1 + 2\mathcal{A} \cos \bar{I} + \mathcal{A}^2 \right)^{1/2}, \quad (46)$$

from which we obtain

$$\left| \frac{\dot{\bar{I}}_e}{\bar{\Omega}_e} \right| = \left( \frac{\mathcal{A}}{\bar{\mathcal{A}}} \right) \frac{1}{\left| \bar{\Omega}_{\text{L}} \right|} \frac{\mathcal{A} \sin \bar{I}}{(1 + 2\mathcal{A} \cos \bar{I} + \mathcal{A}^2)^{3/2}}. \quad (47)$$

<sup>2</sup> Given the complicated evolution of  $\bar{\Omega}_e$  and  $\dot{\bar{I}}_e$ , it is difficult to give a more exact bound on the deviation from adiabaticity. In practice, deviations  $\lesssim 1^\circ$  are observationally indistinguishable, so the exact scaling in this regime is negligible.

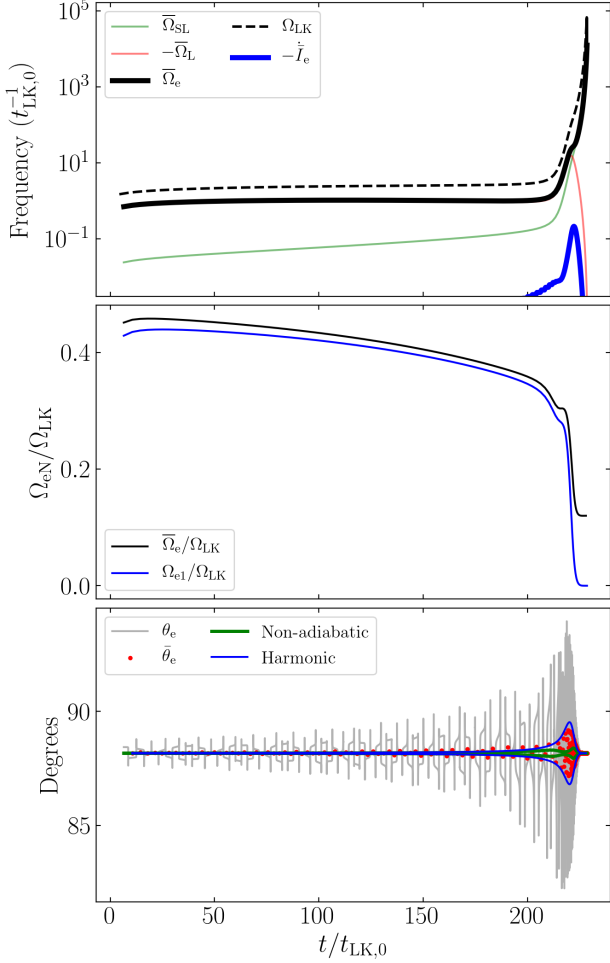


**Figure 5.** The same simulation as Fig. 1 but showing calculated quantities relevant to the theory of the paper over the course of the simulation. Top: the important frequencies of the system. Middle: the frequency ratios between the zeroth and first Fourier components of  $\Omega_e$  to the LK frequency  $\Omega_{LK}$ . Bottom: Plot of  $\theta_e$  [grey; Eq. (28)],  $\bar{\theta}_e$  [red dots; Eq. (38)], as well as estimates of the deviations from perfect conservation of  $\bar{\theta}_e$  due to non-adiabatic effects [green, Eq. (43)] and due to resonances with harmonic terms [blue, Eq. (63)].

Moreover, if we approximate  $e \approx 1$  and  $\cos^2 \omega \approx 1/2$  in  $d\bar{\Omega}/dt$ , we can estimate

$$\mathcal{A} \approx \frac{3Gn(m_2 + \mu/3)}{2c^2 a j^2} \left[ \frac{15 \cos \bar{I}}{8 t_{LK} j} \right]^{-1}, \quad (48)$$

$$\approx \frac{4}{5} \frac{G(m_2 + \mu/3)m_{12}\tilde{a}_3^3}{c^2 m_3 a^4 j \cos \bar{I}}, \quad (49)$$

$$\frac{\dot{\mathcal{A}}}{\mathcal{A}} = -4 \left( \frac{\dot{a}}{a} \right)_{\text{GW}} + \frac{e}{j^2} \left( \frac{de}{dt} \right)_{\text{GW}}. \quad (50)$$

With this, we see that Eq. (47) is small except when  $\mathcal{A} \approx 1$ , and so we obtain that the maximum  $\dot{I}_e/\bar{\Omega}_e$  is given roughly

by

$$\left| \frac{\dot{I}_e}{\bar{\Omega}_e} \right|_{\text{max}} \approx \left( \frac{\dot{\mathcal{A}}}{\mathcal{A}} \right) \frac{1}{\left| \frac{\dot{\mathcal{A}}}{\mathcal{A}} \right|} \frac{\sin \bar{I}}{(2 + 2 \cos \bar{I})^{3/2}}. \quad (51)$$

To evaluate this, we make two assumptions: (i)  $\bar{I}$  is approximately constant (see third panels of Figs. 6 and 7), and (ii)  $j(e)$  evaluated at  $\mathcal{A} \approx 1$  can be approximated as a constant multiple of the initial  $j(e_{\text{max}})$ , so that

$$j_{\star} \equiv j(e_{\star}) = f \sqrt{\frac{5}{3} \cos^2 I_0}, \quad (52)$$

for some unknown factor  $f > 1$ ; we use star subscripts to denote evaluation at  $\mathcal{A} \approx 1$ .  $f$  turns out to be relatively insensitive to  $I_0$ . This can be as systems with lower  $e_{\text{max}}$  values taking more cycles to attain  $\mathcal{A} \approx 1$ , resulting in all systems experiencing a similar amount of decay due to GW radiation.

For simplicity, let's first assume  $\mathcal{A} \approx 1$  is satisfied when the LK oscillations are mostly suppressed, and  $e_{\star} \approx 1$  is a constant throughout the LK cycle (see second panels of Figs. 6 and 7; we will later see that the scalings are the same in the LK-oscillating regime). Approximating  $e_{\star} \approx 1$  in Eqs. (10) and (11) gives

$$\left[ \frac{\dot{\mathcal{A}}}{\mathcal{A}} \right]_{\star} \approx \frac{G^3 \mu m_{12}^2}{c^5 a_{\star}^4 j_{\star}^7} \frac{595}{3}. \quad (53)$$

Again assuming  $e_{\star} \approx 1$  and averaging  $\cos^2 \omega \approx 1/2$  in  $d\bar{\Omega}/dt$  Eq. (5) gives

$$\bar{\Omega}_{L,\star} \approx \frac{15 \cos \bar{I}}{8 t_{LK,\star} j_{\star}}. \quad (54)$$

Lastly, to fix  $a_{\star}$ , we require Eq. (49) to give  $\mathcal{A} = 1$  for  $a_{\star}$  and  $j_{\star}$ . Taking all of these together, we obtain

$$\left| \frac{\dot{I}_e}{\bar{\Omega}_e} \right|_{\text{max}} \approx \frac{952}{9} \frac{G^3 \mu m_{12}^3 \tilde{a}_3^3}{c^5 \sqrt{G} m_{12} m_3} \left( \frac{5c^2 m_3 \cos \bar{I}}{4G(m_2 + \mu/3)m_{12}\tilde{a}_3^3} \right)^{11/8} \times (j_{\star})^{-37/8} \frac{\tan \bar{I}}{(2 + 2 \cos \bar{I})^{3/2}}, \quad (55)$$

$$\approx XXX \left( \frac{\tilde{a}_3}{2.2 \text{ pc}} \right)^{-9/8} \dots \quad (56)$$

We take constant  $\bar{I} = 120^\circ$  (Figs. 6 and 7 show that this is a serviceable approximation that holds across a range of  $I_0$ ). Then Eq. (56) has only one free parameter,  $f$ , which enters through  $j_{\star}$  following Eq. (52). We can also calculate  $\dot{I}_e/\bar{\Omega}_e$  from numerical simulations. Fitting  $f$  to the data from numerical simulations gives  $f = 2.6$ . The result of this fit is shown in Fig. 8, where it is clear the scaling predicted by Eq. (56) is remarkably accurate.

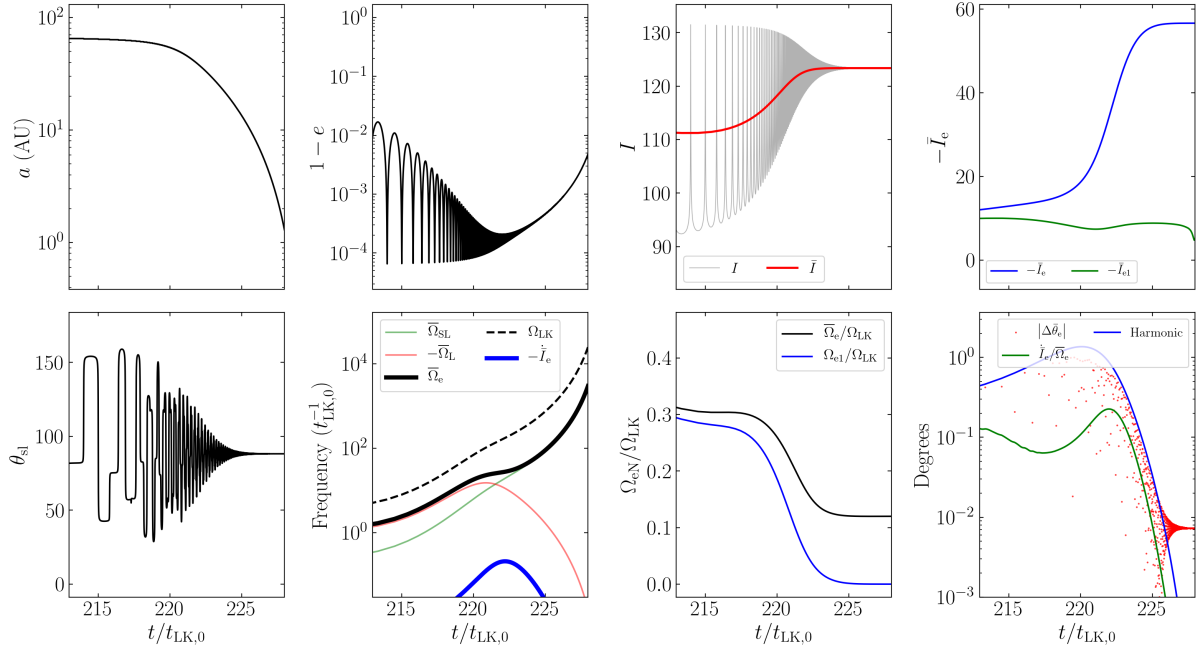


**Figure 6.** The same simulation as Fig. 1 but shown focusing on the region where  $\mathcal{A} \approx 1$ . The first three panels depict  $a$ ,  $e$ ,  $I$  and  $\bar{I}$  as before, while the fourth shows  $I_e$  [Eq. (32)] and  $I_{e1}$ . The bottom four panels depict  $\theta_{sl}$ ; the five characteristic frequencies of the system [Eqs. 25 and (26)]; and the same quantities as the top and bottom panels of Fig. 5. In the final panel, it is clear that oscillations in  $\bar{\theta}_e$  are dominantly driven by interactions with the  $N = 1$  harmonic.

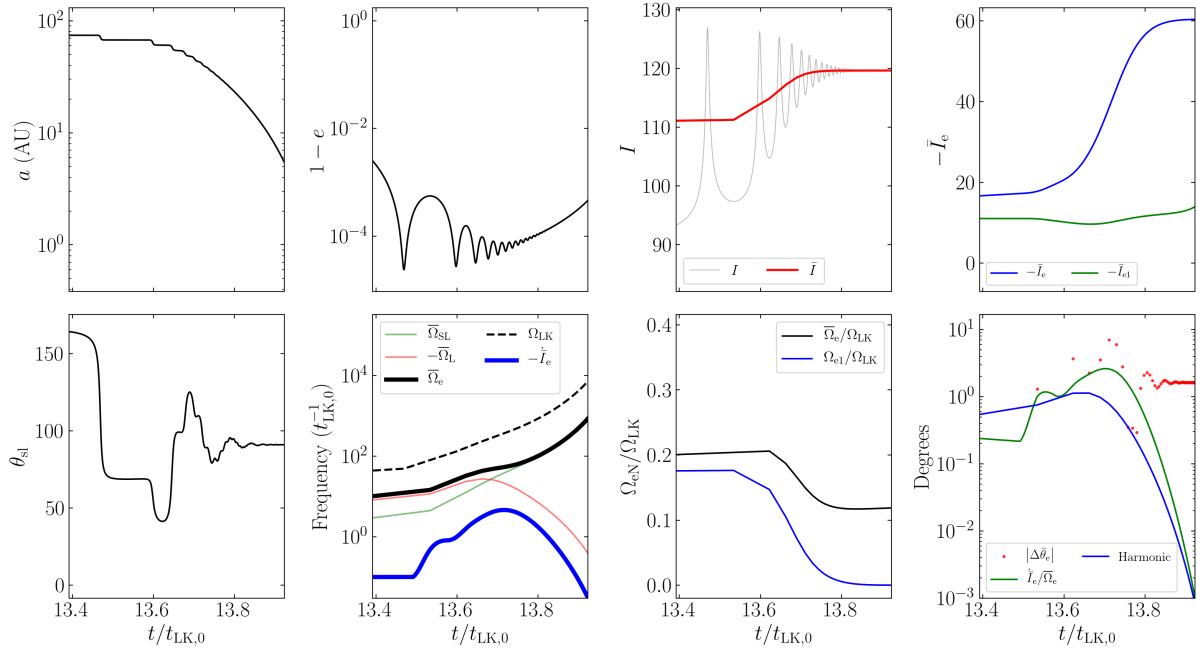


**Figure 7.** Same as Fig. 6 except for  $I_0 = 90.2^\circ$ , corresponding to a faster coalescence and a total change in  $\bar{\theta}_e$  of  $\approx 2^\circ$ . In the bottom middle panel, the nonadiabatic contribution is more significant and causes much poorer conservation of  $\bar{\theta}_e$ .



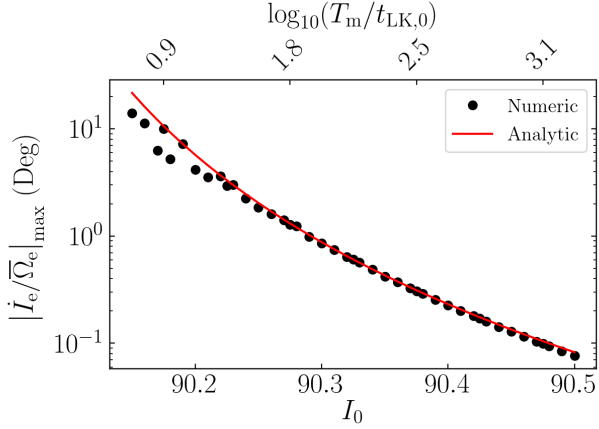


**Figure 8.** Comparison of  $|\dot{I}_e/\bar{\Omega}_e|_{\max}$  extracted from simulations and using Eq. (56), where we take  $f = 2.6$  in Eq. (52). The coalescence time  $T_m$  is shown along the top axis of the plot in units of the characteristic LK timescale at the start of inspiral  $t_{\text{LK},0}$ ; the LK period is initially of order a few  $t_{\text{LK},0}$ . The agreement is remarkable for systems that coalesce over many  $t_{\text{LK},0}$ .

Above, we assumed that the system evolves through  $\mathcal{A} \simeq 1$  when the eccentricity is mostly frozen (see Fig. 1 for an indication of how accurate this is for the parameter space explored in Fig. 8). It is also possible that  $\mathcal{A} \simeq 1$  occurs when the eccentricity is still undergoing substantial oscillations. In fact, Eq. (56) is still accurate in this regime when replacing  $e$  with  $e_{\max}$ , due to the following analysis. Recall that when  $e_{\min} \ll e_{\max}$ , the binary spends a fraction  $\sim j(e_{\max})$  of the LK cycle near  $e \simeq e_{\max}$  (Anderson et al. 2016). This fraction of the LK cycle dominates both GW dissipation and  $\bar{\Omega}_e$  precession. Thus, both  $\dot{I}_e$  and  $\bar{\Omega}_e$  in the oscillating- $e$  regime are evaluated by setting  $e \simeq e_{\max}$  and adding a prefactor of  $j(e_{\max})$ . The prefactors of  $j(e_{\max})$  cancel when computing the quotient  $\dot{I}_e/\bar{\Omega}_e$ .

The accuracy of Eq. (56) in bounding  $|\Delta\bar{\theta}_e|^f$  is shown in Fig. 9. Note that conservation of  $\bar{\theta}_e$  is generally much better than Eq. (56) predicts. This is because cancellation of phases in Eq. (42) is generally more efficient than Eq. (56) assumes.

#### 4.4. $\theta_{\text{sl}}^f$ Behavior

In Fig. 2, we plotted  $\theta_{\text{sl}}^f$  as a function of  $I_0$  when  $\theta_{\text{sl}}^i = 0$ . With the results developed in the previous sections, we can understand very well the behavior seen in this plot.

Note that, for the fiducial parameter space,  $\bar{\Omega}_L \gg \bar{\Omega}_{\text{SL}}$  initially (Fig. 5), and so by Eq. (25) we have

$$\frac{\bar{\Omega}_e}{\bar{\Omega}_e} \approx \text{sgn}(\bar{\Omega}_L) \hat{\mathbf{L}}_{\text{out}}. \quad (57)$$

If then  $\theta_{\text{sl}}^i = 0^\circ$ , we have  $\bar{\theta}_e^i \approx I_0$ , and when  $\bar{\theta}_e$  is conserved, we obtain the desired result  $\bar{\theta}_e^f = \theta_{\text{sl}}^f \approx 90^\circ$ . Note that this

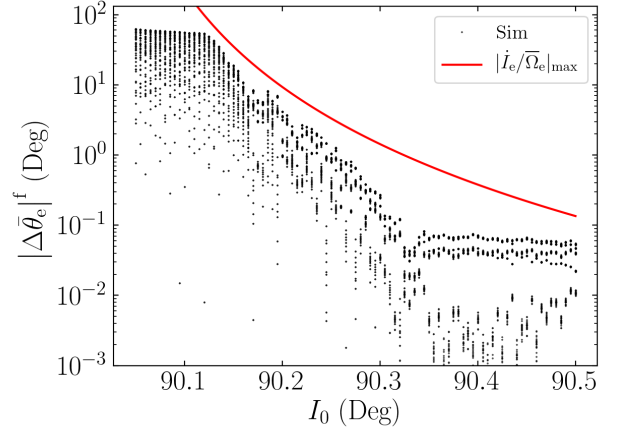


**Figure 9.** Total change in  $\bar{\theta}_e$  over inspiral as a function of initial inclination  $I_0$ , where the initial  $\bar{\Omega}_e$  is computed without GW dissipation. For each  $I_0$ , 100 simulations are run for  $\mathbf{S}$  on a uniform, isotropic grid. Plotted for comparison is the bound  $|\Delta\bar{\theta}_e|^f \lesssim |\dot{I}_e/\bar{\Omega}_e|_{\max}$ , using the analytical scaling given by Eq. (56). It is clear that the given bound is not tight but provides an upper bound for non-conservation of  $\bar{\theta}_e$  due to nonadiabatic effects. At the right of the plot, the accuracy saturates: this is because neglecting GW dissipation causes inaccuracies when computing the average  $\bar{\Omega}_e$ .

is a general feature for LK-induced mergers if  $\theta_{\text{sl}}^i = 0^\circ$ , since  $I_0 \approx 90^\circ$  is required for sufficient  $e$ -excitation to cause the binary to merge. Careful examination of Fig. 2 shows the  $\theta_{\text{sl}}^f$  values for slower mergers is slightly below  $90^\circ$ . This is because  $\bar{\Omega}_e$  differs slightly from  $\mathbf{L}_{\text{out}}$  when  $\bar{\Omega}_{\text{SL}}$  is nonzero, and indeed  $\bar{\theta}_e \approx 88.5^\circ$  for  $I_0 = 90.5^\circ$  and  $I_0 = 89.5^\circ$ .

This also reproduces a recent result that  $\theta_{\text{sl}}^f$  either equals  $\theta_{\text{sb}}^i$  or  $180^\circ - \theta_{\text{sb}}^i$ , where  $\theta_{\text{sb}}^i$  is the initial angle between  $\mathbf{L}_{\text{out}}$  and  $\mathbf{S}$  (Yu et al. 2020). Noting  $\text{sgn}(\bar{\Omega}_L)$  is positive for  $I_0 < 90^\circ$  and negative for  $I_0 > 90^\circ$ , we get

$$\bar{\theta}_e^i \approx \begin{cases} \theta_{\text{sb}}^i & I_0 < 90^\circ, \\ 180^\circ - \theta_{\text{sb}}^i & I_0 > 90^\circ, \end{cases} \quad (58)$$

Following the above analysis,  $\bar{\theta}_e$  conservation then immediately gives

$$\theta_{\text{sl}}^f \approx \begin{cases} \theta_{\text{sb}}^i & I_0 < 90^\circ, \\ 180^\circ - \theta_{\text{sb}}^i & I_0 > 90^\circ. \end{cases} \quad (59)$$

Having understood the behavior of the  $\theta_{\text{sl}}^f$  distribution for adiabatic mergers and the  $90^\circ$  attractor, we next turn to the structure of the deviations in Fig. 2. The deviations grow towards  $I_0 = 90^\circ$ . This follows the shape predicted by Eq. (56) and shown in Fig. 9. The oscillatory nature of these deviations can also be understood: Eq. (44) only gives the maximum of the absolute value of the change in  $\bar{\theta}_e$ , while the actual change

depends on the initial and final complex phases, denoted  $\Phi(t_i)$  and  $\Phi(t_f)$ . When  $\theta_{sl}^i = 0$ , we have  $\Phi(t_i) = 0$ , as  $\mathbf{S}$  starts in the  $\hat{\mathbf{x}}\text{-}\hat{\mathbf{z}}$  plane. Then, as  $I_0$  is smoothly varied, the final phase  $\Phi(t_f)$  will also smoothly vary, so the total phase difference between the initial and final values of  $S_\perp$  vary smoothly. This means the total change in  $\bar{\theta}_e$  will fluctuate smoothly between  $\pm |\Delta\bar{\theta}_e|^f$  as  $I_0$  is smoothly varied, giving rise to the sinusoidal shape seen in Fig. 2.

### 5. ANALYSIS: EFFECT OF RESONANCES

In the previous section, we neglected the  $N \geq 1$  Fourier harmonics in Eq. (27), and showed that the final  $\theta_{sl}^f$  behavior could be completely explained. In this section, we study one effect of the Fourier harmonics that occurs when two frequencies become commensurate. We show that, while this effect can be neglected for the fiducial parameter regime, it becomes important to explain some of the results in Liu & Lai (2017). This connection is discussed in Section 6.

For simplicity, we ignore the effects of GW dissipation in this section and assume the system is exactly periodic (so  $\dot{I}_e = 0$ ). The scalar equation of motion Eq. (36) is then:

$$\frac{dS_\perp}{dt} = i\bar{\Omega}_e S_\perp + \sum_{N=1}^{\infty} [\cos(\Delta I_{eN}) S_\perp - i \cos \theta \sin(\Delta I_{eN})] \Omega_{eN} \cos(N\Omega_{LK}t). \quad (60)$$

Resonances can occur when  $\bar{\Omega}_e = N\Omega_{LK}$ . Numerically, we find that  $\bar{\Omega}_e \lesssim \Omega_{LK}$  for most regions of parameter space (see Fig. 10, and recall that LK-induced mergers only complete within a Hubble time when  $I_{\min} \approx 90^\circ$ ). Accordingly, we restrict our analysis to resonances with the  $N = 1$  component. For simplicity, we also ignore the modulation of the forcing frequency in Eq. (60). While this fails to capture the possibility of a parametric resonance, we find no evidence for parametric resonances in our simulations. With these two simplifications, Eq. (60) further reduces to

$$\frac{dS_\perp}{dt} \approx i\bar{\Omega}_e S_\perp - i \cos \bar{\theta}_e \sin(\Delta I_{e1}) \Omega_{e1} \cos(\Omega_{LK}t). \quad (61)$$

We can approximate  $\cos(\Omega_{LK}t) \approx e^{i\Omega_{LK}t}/2$ , as the  $e^{-i\Omega_{LK}t}$  component is far from resonance. Then we can write down solution as before

$$e^{-i\bar{\Omega}_e t} S_\perp \Big|_{t_i}^{t_f} = - \int_{t_i}^{t_f} \frac{i \sin(\Delta I_{e1}) \Omega_{e1}}{2} e^{-i\bar{\Omega}_e \tau + i\Omega_{LK} \tau} \cos \bar{\theta}_e d\tau. \quad (62)$$

Thus, similarly to Section 4.2, the instantaneous oscillation amplitude  $|\Delta\bar{\theta}_e|$  can be bound by

$$|\Delta\bar{\theta}_e| \sim \frac{1}{2} \left| \frac{\sin(\Delta I_{e1}) \Omega_{e1}}{\Omega_{LK} - \bar{\Omega}_e} \right|. \quad (63)$$

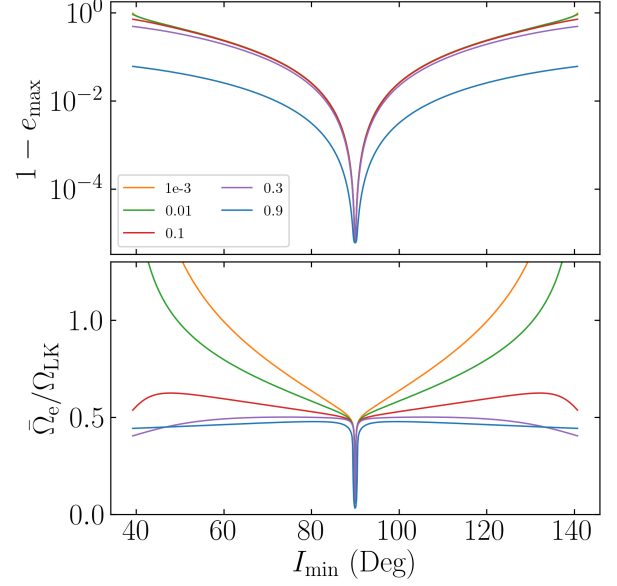


**Figure 10.**  $e_{\max}$  and  $\bar{\Omega}_e/\Omega_{LK}$  as a function of  $I_{\min}$ , the inclination of the inner binary at eccentricity minimum, for varying values of  $e_{\min}$  (different colors) for the fiducial parameter regime.

We see that if  $\bar{\Omega}_e < \Omega_{LK}$  by a sufficient margin for all times, then the conservation of  $\bar{\theta}_e$  in the fiducial parameter regime cannot be significantly affected by this resonance. The ratio  $\bar{\Omega}_e/\Omega_{LK}$  is shown in the middle panel of Fig. 5, and the amplitude of oscillation of  $\bar{\theta}_e$  it generates [Eq. (63)] is given in blue in the bottom panel of Fig. 5. We see that the total effect of the harmonic terms never exceeds a few degrees.

Furthermore, the bottom-rightmost panel of Fig. 6 compares the detailed behavior of  $\bar{\theta}_e$  and its two contributions, the nonadiabatic and harmonic effects in the vicinity of  $\bar{\mathcal{A}} \approx 1$ . We see that Eq. (63) describes the oscillations in  $\bar{\theta}_e$  very well. The agreement is poorer in the bottom-rightmost panel of Fig. 7, as the nonadiabatic effect is much stronger. However, note that the theory presented in the previous section captures the final deviations  $|\Delta\bar{\theta}_e|^f$  very well. This suggests that oscillations in  $\bar{\theta}_e$  due to Eq. (63) of up to a few degrees do not affect final nonconservation by more than  $\sim 0.01^\circ$ .

### 6. LIDOV-KOZAI ENHANCED MERGERS

In Liu & Lai (2017), a different parameter regime is considered, where the inner binary is sufficiently close in ( $\sim 0.1$  AU) that it can merge in isolation via GW radiation, given by:  $m_1 = m_2 = m_3 = 30M_\odot$ ,  $a_{\text{in}} = 0.1$  AU,  $\tilde{a}_3 = 3$  AU, and  $e_3 = 0$ . Note that  $m_3$  here is not an SMBH. However, our results can still be applied judiciously to this parameter regime and yield interesting insights.

First, we recall the  $\theta_{sl}^f$  distribution obtained via numerical simulation, shown in Fig. 11. Liu & Lai (2017) derives an adiabatic invariant assuming the inner binary does not undergo

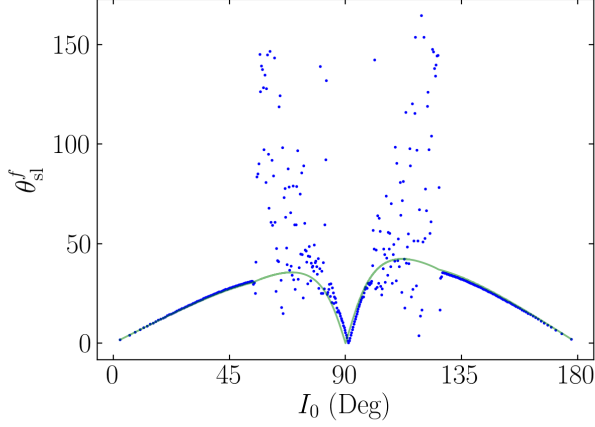


**Figure 11.** Plot of  $\theta_{\text{sl}}^f$  for the LK-enhanced parameter regime, i.e.  $m_1 = m_2 = m_3 = 30M_\odot$ ,  $a_{\text{in}} = 0.1$  AU,  $\tilde{a}_3 = 3$  AU, and  $e_3 = 0$ . Conservation of  $\bar{\theta}_e$  gives the green line. Agreement near  $I_0 = 90^\circ$  is good when accounting for the effects of a finite  $L_{\text{out}}$  (see Fig. 12). For  $I_0$  in the two intervals  $[40^\circ, 80^\circ]$  and  $[100^\circ, 140^\circ]$ , a further effect causes  $\theta_{\text{sl}}^f$  to fluctuate unpredictably.

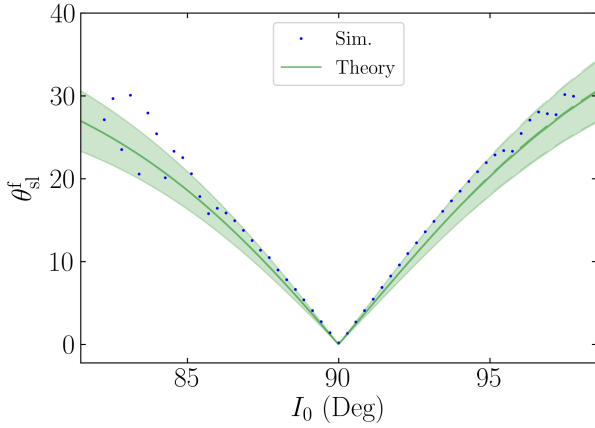


**Figure 12.** Zoomed in version of Fig. 11 near  $I_0 \approx 90^\circ$  while adding an  $I_0$  offset to account for differences between the data and theory due to finite  $L_{\text{out}}$  effects. The green shaded area shows the expected range of deviations due to resonant perturbations following Eq. (63) (evaluated for the initial system parameters). The data nearer  $90^\circ$  have less spread than predicted, but the transition to a larger  $\theta_{\text{sl}}^f$  spread roughly follows the prediction of the green line.

eccentricity oscillations. Our result, based on  $\bar{\theta}_e$  conservation, is a generalization of their result, giving the same result when the inner orbit remains circular. Very near  $I_0 \approx 90^\circ$ , the data are offset somewhat from our result, because we have assumed the tertiary's angular momentum is fixed, but accounting for the offset, our theory captures the scaling of  $\theta_{\text{sl}}^f$ , as seen in Fig. 12.

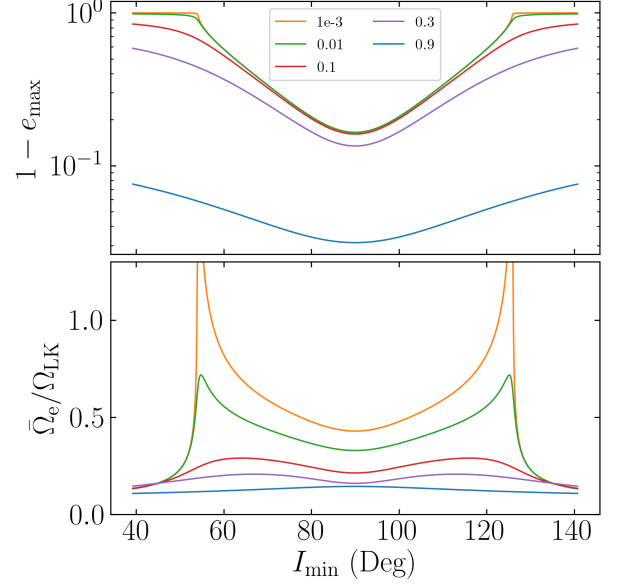


**Figure 13.** Same as Fig. 10 but for the compact parameter regime. Compared to Fig. 10, we see that  $e_{\text{max}}$  is smaller due to stronger pericenter precession  $\Omega_{\text{GR}}$  in this regime, so the  $\bar{\Omega}_e/\Omega_{\text{LK}} = 1$  resonance is accessible for a wide range of parameter space. In particular, both smaller  $e_{\text{min}}$  and  $e_{\text{max}}$  values bring the system closer to the resonance.

However, as can be seen in Fig. 11, intermediate inclinations  $I_0 \in [50, 80]$  and  $I_0 \in [100, 130]$  exhibit very volatile behavior in  $\theta_{\text{sl}}^f$ . This is unlike the plots generated in the fiducial parameter regime (Fig. 2), as this inclination regime corresponds to neither the fastest nor slowest merging systems. We attribute the origin of this volatility to a stronger resonant interaction. By examining Fig. 13, it is evident that, for the same  $e_{\text{min}}$ , systems with  $I_{\text{min}}$  further from  $90^\circ$  are closer to the  $\bar{\Omega}_e = \Omega_{\text{LK}}$  resonance. Outside of the LK window,  $\bar{\Omega}_e$  also goes swiftly to zero, as seen in Fig. 13, so this explanation is consistent with the ranges of inclinations that exhibit volatile  $\theta_{\text{sl}}^f$  behavior. We forgo further investigation of this mechanism because it is not expected to play an important role in any LK-induced BH binary mergers for reasons discussed below.

At first, it seems clear from Fig. 10 that  $\bar{\Omega}_e$  is significantly smaller than  $\Omega_{\text{LK}}$  near  $I_{\text{min}} \approx 90^\circ$  for LK-induced mergers. However, this is not sufficient to guarantee that the frequency ratio remains small for the entire evolution, as GR effects become stronger as the binary coalesces. Instead, a more careful analysis of the relevant quantities in Eq. (63) proves useful:

- $\sin(\Delta I_{e1})$  is small unless  $\mathcal{A} \approx 1$ . Otherwise,  $\Omega_e$  does not nutate appreciably within an LK cycle, and all the  $\Omega_{eN}$  are aligned with  $\bar{\Omega}_e$ , implying all the  $\Delta I_{eN} \approx 0$ .

- Smaller values of  $e_{\min}$  increase  $\bar{\Omega}_e/\Omega_{\text{LK}}$ , as shown in Fig. 13.

However, LK-driven coalescence causes  $\mathcal{A}$  to increase on a similar timescale to that of  $e_{\min}$  increase (see Fig. 1). This implies that, if  $\mathcal{A} \ll 1$  initially, which is the case for LK-induced mergers, then  $e_{\min}$  will be very close to 1 when  $\mathcal{A}$  grows to be  $\simeq 1$ , and the contribution predicted by Eq. (63) must be small.

## 7. CONCLUSION AND DISCUSSION

In this paper, we consider the evolution of the spin-orbit misalignment angle  $\theta_{\text{sl}}$  of a black hole (BH) binary that merges under gravitational wave (GW) radiation during Lidov-Kozai (LK) oscillations induced by a tertiary supermassive black hole (SMBH). We show that, when the gravitational potential of the SMBH is handled at quadrupolar order, the spin vectors of the inner BHs obey the simple equa-

tion of motion Eq. (24). Analysis of this equation yields the following conclusions:

- Since Eq. (24) is a linear system with periodically varying coefficients, it cannot give rise to chaotic dynamics by Floquet’s Theorem.
- For most parameters of astrophysical relevance, the angle  $\bar{\theta}_e$  [Eq. (38)] is an adiabatic invariant. Since the inner BH binary merges in finite time,  $\bar{\theta}_e$  is only conserved to finite accuracy; we show that the deviation from perfect adiabaticity can be predicted from initial conditions.
- When the resonant condition  $\bar{\Omega}_e \approx \Omega_{\text{LK}}$  is satisfied, significant oscillations in  $\bar{\theta}_e$  can arise. We derive an analytic estimate of this oscillation amplitude. This estimate both demonstrates that the resonance is unimportant for “LK-induced” mergers and tentatively explains the scatter in  $\theta_{\text{sl}}^f$  seen by Liu & Lai (2017).

## REFERENCES

- Abbott, B., et al. 2016a, Phys. Rev. X, 6, 041015, doi: [10.1103/PhysRevX.6.041015](https://doi.org/10.1103/PhysRevX.6.041015)
- . 2016b, Phys. Rev. Lett., 116, 061102, doi: [10.1103/PhysRevLett.116.061102](https://doi.org/10.1103/PhysRevLett.116.061102)
- . 2017a, Phys. Rev. Lett., 119, 141101, doi: [10.1103/PhysRevLett.119.141101](https://doi.org/10.1103/PhysRevLett.119.141101)
- Abbott, B. P., et al. 2016c, Phys. Rev. Lett., 116, 241103, doi: [10.1103/PhysRevLett.116.241103](https://doi.org/10.1103/PhysRevLett.116.241103)
- . 2017b, Astrophys. J., 851, L35, doi: [10.3847/2041-8213/aa9f0c](https://doi.org/10.3847/2041-8213/aa9f0c)
- . 2017c, Phys. Rev. Lett., 118, 221101, doi: [10.1103/PhysRevLett.118.221101](https://doi.org/10.1103/PhysRevLett.118.221101)
- Abbott, R., et al. 2020, arXiv preprint arXiv:2004.08342, <https://arxiv.org/abs/2004.08342>
- Anderson, K. R., Storch, N. I., & Lai, D. 2016, Monthly Notices of the Royal Astronomical Society, 456, 3671
- Dominik, M., Belczynski, K., Fryer, C., et al. 2012, The Astrophysical Journal, 759, 52
- Fuller, J., & Ma, L. 2019, The Astrophysical Journal Letters, 881, L1
- Graham, M. J., Ford, K. E. S., McKernan, B., et al. 2020, Phys. Rev. Lett., 124, 251102, doi: [10.1103/PhysRevLett.124.251102](https://doi.org/10.1103/PhysRevLett.124.251102)
- Kinoshita, H. 1993, Celestial Mechanics and Dynamical Astronomy, 57, 359
- Kozai, Y. 1962, The Astronomical Journal, 67, 591
- Lidov, M. L. 1962, Planetary and Space Science, 9, 719
- Liu, B., & Lai, D. 2017, The Astrophysical Journal Letters, 846, L11
- . 2018, The Astrophysical Journal, 863, 68
- Peters, P. C. 1964, Physical Review, 136, B1224
- Storch, N. I., & Lai, D. 2015, Monthly Notices of the Royal Astronomical Society, 448, 1821
- Yu, H., Ma, S., Giesler, M., & Chen, Y. 2020, arXiv preprint arXiv:2007.12978